

Reversible Redox Cycling of Well-Defined, Ultrasmall Cu/Cu₂O Nanoparticles

Sebastian D. Pike,[†] Edward R. White,[†] Anna Regoutz,[‡] Nicholas Sammy,[†] David J. Payne,[‡] Charlotte K. Williams,^{*,§} and Milo S. P. Shaffer^{*,†,‡}

[†]Department of Chemistry, Imperial College London, Imperial College Road, London SW7 2AZ, U.K.

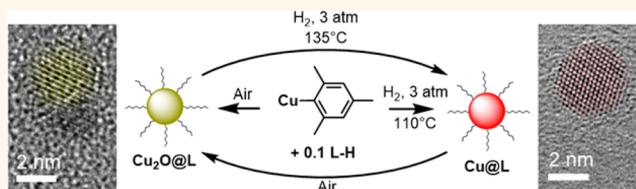
[‡]Department of Materials, Imperial College London, Imperial College Road, London SW7 2AZ, U.K.

[§]Department of Chemistry, Oxford University, Chemistry Research Laboratory, 12 Mansfield Road, Oxford OX1 3TA, U.K.

Supporting Information

ABSTRACT: Exceptionally small and well-defined copper (Cu) and cuprite (Cu₂O) nanoparticles (NPs) are synthesized by the reaction of mesitylcopper(I) with either H₂ or air, respectively. In the presence of substoichiometric quantities of ligands, namely, stearic or di(octyl)phosphinic acid (0.1–0.2 equiv vs Cu), ultrasmall nanoparticles are prepared with diameters as low as ~2 nm, soluble in a range of solvents. The solutions of Cu NPs undergo quantitative oxidation, on exposure to air, to form Cu₂O NPs. The Cu₂O NPs can be reduced back to Cu(0) NPs using accessible temperatures and low pressures of hydrogen (135 °C, 3 bar H₂). This striking reversible redox cycling of the discrete, solubilized Cu/Cu(I) colloids was successfully repeated over 10 cycles, representing 19 separate reactions. The ligands influence the evolution of both composition and size of the nanoparticles, during synthesis and redox cycling, as explored in detail using vacuum-transfer aberration-corrected transmission electron microscopy, X-ray photoelectron spectroscopy, and visible spectroscopy.

KEYWORDS: organo-copper(I), copper nanoparticles, copper(I) oxide nanoparticles, redox switching, ultrasmall nanoparticles, transmission electron microscopy



Copper nanoparticles (Cu NPs) have wide applications ranging from photonic materials for surface-enhanced spectroscopies and imaging techniques¹ to conductive inks for microelectronics^{2–4} and as catalysts.^{5–10} Ultrasmall NPs (*i.e.*, particles in the size regime of 1–3 nm) are of particular interest due to their very high surface areas and small internal volumes, which lead to modified intrinsic properties compared to larger NPs.^{4,11} Copper NPs could also be an attractive replacement for the heavier congeners, silver and gold, for reasons of the elemental abundance and relatively low cost. However, their rapid oxidation, upon exposure to air, remains a major practical limitation. Coordinating ligands, or surfactants, can provide a kinetic barrier to oxidation,^{12,13} though more robust protection, over prolonged periods or at elevated temperatures, requires a surface layer of a more stable oxide, such as Al₂O₃.¹⁴ However, surface-passivated particles have limited utility because the metallic copper surface is isolated. Our goal is to develop a rapid and reversible redox reaction, interconverting between Cu and Cu₂O NPs, thereby allowing facile regeneration of Cu NPs at the point of application.

Although, under ambient conditions, CuO (monoclinic lattice) is the thermodynamically preferred bulk oxide of copper, Cu₂O (face-centered cubic (fcc) Cu lattice) is more stable at the nanoscale; small Cu NPs (<25 nm) oxidize under

air to stable Cu₂O NPs.^{12,13,15–22} Diffusion of oxygen into the fcc copper lattice induces a simple lattice expansion to form Cu₂O (volume increase ~65%),¹³ while retaining the same lattice symmetry; in contrast, the formation of monoclinic CuO requires significant disruption to the lattice.^{23,24} Cu₂O is itself a useful semiconducting material with a direct band gap of ~2.2 eV²⁵ and has been applied in photocatalysis,^{26–29} photovoltaics,^{22,30,31} cross-coupling catalysis,^{20,32,33} gas sensors,³⁴ and nanofluidics for solar water heating.³⁵ Most syntheses of Cu₂O NPs produce larger diameters (*e.g.*, 4–25 nm),^{24,29,36} and although Cu₂O ultrasmall NPs (<3 nm) are known,³⁷ simple, scalable routes for their synthesis remain an interesting target.

The oxidation of Cu NPs to form Cu₂O NPs is well-known;^{12,13,15–22} however, the reduction of Cu₂O NPs back to Cu NPs, as required for redox cycling, is much less studied, particularly in solution.^{20,21,38–43} Many catalytic processes involve the reduction of copper oxides as a means to form active copper sites, but these reactions are not fully understood and generally occur on solid-supported heterogeneous catalysts.^{40,44,45} Yanase *et al.* reported, as early as 1991, that solid-supported Cu NPs (5–15 nm) could be oxidized in air to

Received: November 15, 2016

Accepted: March 7, 2017

Published: March 13, 2017

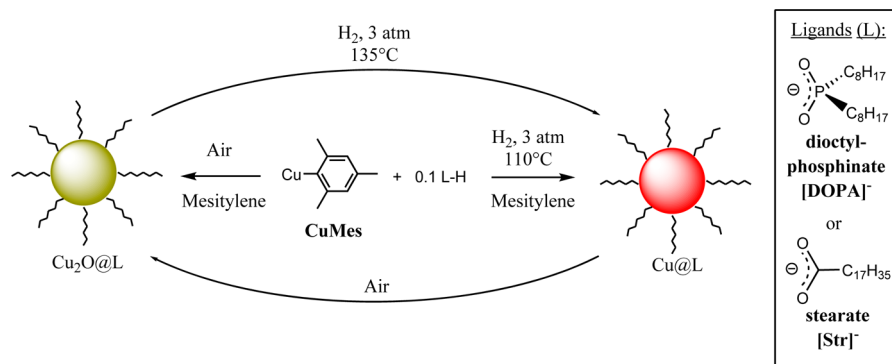


Figure 1. Synthesis of Cu NPs and Cu₂O NPs from CuMes (L-H = Str-H or DOPA-H; for suggestions for “molecular” formulas of typically sized NPs and balanced equations, see [Supporting Note 3](#)).

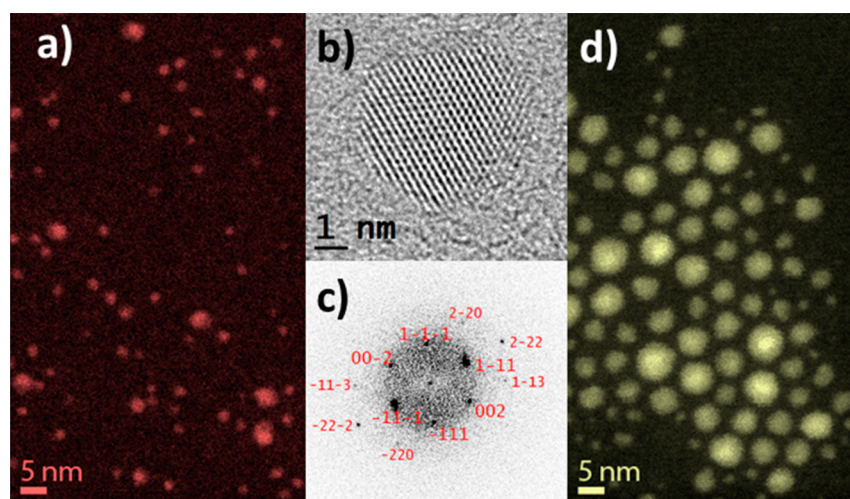


Figure 2. (a) Annular dark-field scanning TEM (ADF-STEM) image of Cu@DOPA NPs. (b) HRTEM image of a single Cu@DOPA NP (both a and b using a vacuum transfer holder to prevent exposure to atmospheric oxygen). (c) Fourier transform of image (b) showing diffraction spots consistent with Cu FCC lattice. (d) ADF-STEM image of NPs after oxidation in air, where they have transformed into Cu₂O@DOPA (a and d at same scale).

CuO/Cu₂O and subsequently re-reduced at high temperatures using H₂.^{38,39} After several reduction reactions, substantial migration of Cu atoms onto the support decreased the size of the remaining Cu(0) NPs. More recently, Cu@hexadecylamine NPs (~8 nm) were oxidized in air to give Cu@Cu₂O core-shell particles and subsequently re-reduced using CO gas to reform similar Cu NPs²¹ after this single redox cycle. More generally, the oxidation/reduction of metal NPs has mostly been studied on supported systems at high temperatures (e.g., Rh,⁴⁶ Pd,⁴⁷ or Pt⁴⁸); NP oxidation is associated with lattice expansion⁴⁹ and may also lead to the formation of polycrystallinity or twinning.^{46,47} Reduction of these polycrystalline aggregates can re-form the metal NP with a high degree of surface roughness, potentially advantageous in catalytic processes. In the solution phase, oxidation of metallic iron, cobalt, or nickel NPs can generate hollow sphere metal oxide NPs *via* the Kirkendall effect.^{50–52}

This paper develops efficient routes to prepare both Cu₂O and Cu NP solutions and explores their interconversion over extended redox cycling reactions. Ultrasmall NPs are excellent candidates for both fundamental rapid redox switching studies and many applications due to their high surface areas. For redox switching, the structural similarity of the metallic copper and Cu₂O lattices is appealing, but the formation of stable ultrasmall

NPs is challenging. The organo-copper(I) reagent, mesitylcopper(I) (CuMes), is a promising precursor for Cu NPs;⁵³ reduction using hydrogen at moderate temperatures produces clean products without coordinating organic by-products, allowing independent control over ligating additives.^{17,54} Excess neutral amine ligands can stabilize such Cu NPs, but at low ligand loadings, desirable for applications requiring accessible nanoparticle surfaces, the diameter polydispersity increases.¹⁷ Here, monoanionic ligands, di-(octyl)phosphinate ([DOPA]⁻ = [(C₈H₁₇)₂PO₂]⁻) and stearate ([Str]⁻ = [C₁₇H₃₅CO₂]⁻) ligands, are applied to stabilize the NPs, building on experience with related colloidal methanol synthesis catalysts.^{5,6,55} The bidentate ligands are expected to coordinate strongly to both metal and oxidized NPs by forming strong covalent bonds with the surfaces, which are further strengthened by the chelate effect.

RESULTS AND DISCUSSION

Cu NP Synthesis. Cu NPs were synthesized by the reaction of CuMes ([CuMes] = 0.036 M in mesitylene), with substoichiometric quantities of the appropriate acid, under moderate pressures of hydrogen gas (3 bar) at 110 °C. In contrast to the large majority of NP syntheses, which apply excess ligand or surfactant, here, loadings as low as 0.1 molar

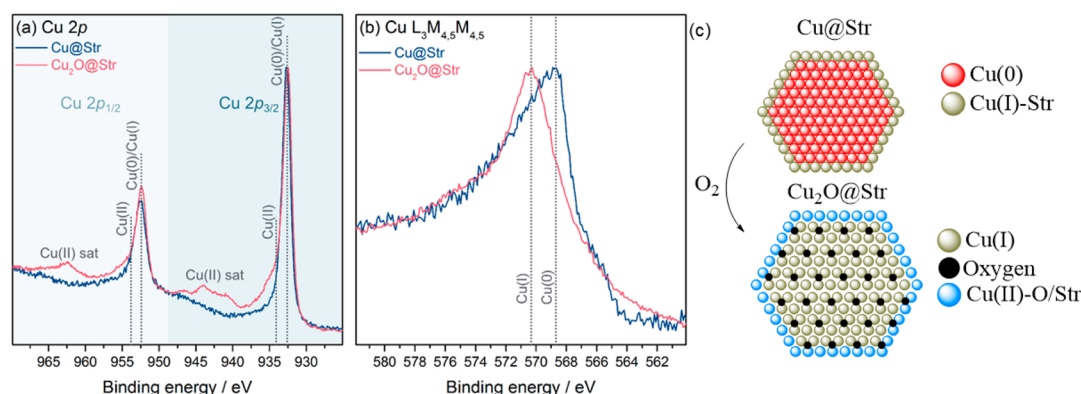


Figure 3. X-ray photoelectron spectra of Cu@Str and Cu₂O@Str samples including (a) Cu 2p core level, (b) Cu L₃M_{4,5}M_{4,5} Auger line, (c) schematic to show possible arrangement of Cu oxidation states in ~ 2 nm Cu@Str and Cu₂O@Str NPs [sketch of a (111) plane].

equiv of ligand *versus* metal precursor were applied to minimize contamination. ¹H and ³¹P (for [DOPA][−]) NMR spectroscopy of the initial reaction mixtures indicated the formation of 0.1 molar equiv of Cu-L type complexes (L = [Str][−] or [DOPA][−]), with quantitative production of mesitylene as the byproduct (Figures S1 and S2). Upon reduction, these mixed solutions of CuMes and Cu-L complexes turned a deep red color, characteristic of Cu NPs, over approximately 1 h. NMR analyses of the product showed broadened resonances consistent with ligands coordinated to NP surfaces.¹³ The complete consumption of reagents to give Cu@L was evident after 2.5 h reaction by NMR spectroscopy (Figures S3 and S4) and confirmed by elemental analyses of dried samples. The products after reaction with the [DOPA][−] ligand were investigated using transmission electron microscopy (TEM), using a vacuum transfer holder to prevent exposure to atmospheric oxygen. The sample showed the formation of small metallic Cu@L NPs, with the majority ($\sim 86\%$) of particles showing ultrasmall diameters of 2 ± 1 nm, although a minor population ($\sim 14\%$) of particles showed larger diameters of 3–6 nm (Figures 2a–c and S5). The particles synthesized using the [Str][−] ligand showed larger average particle sizes of ~ 5 nm (Figure S6). Assuming that all the ligand is bound, the diameters are broadly consistent with the formation of a ligand monolayer (expected particle diameters with a monolayer coverage are 2.9 nm ([DOPA][−]) and 3.5 nm ([Str][−]); see Supporting Notes 2 and 3). Powder X-ray diffraction (XRD) analysis, under anaerobic conditions, of a dried sample of Cu@Str showed the expected pattern for (fcc) metallic Cu [(111), (200), and (220) reflections identified, Figure S7], with a crystallite size of ~ 3.3 nm estimated *via* the Scherrer equation. The smaller size measured by XRD compared to TEM is consistent with the presence of twin or grain boundaries within the nanocrystals, as can often be identified by high-resolution (HR) TEM (Figure S8).²⁴ XRD also showed low-intensity signals indexed to Cu₂O, attributed to trace oxidation of the sample despite sealing with adhesive polyimide tape. In line with this hypothesis, the Cu₂O peaks increased in intensity when the XRD sample was exposed to air for 30 min and were the only features after the dried solid Cu@Str particles were exposed to air for 2 weeks (Figure S7). Visible spectroscopy of Cu@L NP solutions showed surface plasmon resonance (SPR) peaks centered at 566–574 nm, consistent with the formation of small Cu NPs (Figure S9).^{15–18} The Fourier transform infrared (FTIR) spectrum of a carefully dried sample of Cu@Str, handled using anaerobic techniques, showed two signals for

the carboxylate ligand. The features are consistent with a delocalized, monoanionic coordination by the carboxylate to the copper surface (Figure S10). X-ray photoelectron spectroscopy (XPS), where the sample was transferred using a glovebox transfer module to exclude oxygen, confirmed the presence of both the Cu(0) and the stearate ligand (Figures 4 and S11). The Cu 2p core level showed a single contribution at 932.7 eV which can be assigned to either Cu(0) or Cu(I).^{56,57} No shakeup features of the main core line were observed due to the completely filled 3d shells in Cu(0) and Cu(I). A distinction between Cu(0) and Cu(I) cannot be made from the core level alone; however, more information can be extracted from the Cu L₃M_{4,5}M_{4,5} Auger line. The main contribution to the Auger line stems from metallic Cu, with a shoulder to the higher binding energy (BE) side assigned to Cu(I). No evidence for Cu(II) was found in either of the spectra. The XPS measurements confirm that the sample contained a mixture of both Cu(0) and Cu(I). Both XPS and IR data suggest that the particles are surrounded by a surface layer of stearate coordinated to Cu(I) centers around a metallic Cu core (Figures 3 and S11).

Oxidation of Cu NPs to Cu₂O NPs. The Cu NP solutions, in either mesitylene or toluene, oxidized rapidly in air to give green solutions within 10 min; spectroscopically, there was an immediate red shift of the SPR, due to the change in surface polarizability of the metal as the oxide layer forms.^{13,15–18} The SPR intensity continued to drop rapidly as the oxidation proceeded, consistent with other reports of the formation of small Cu₂O NPs (*e.g.*, <5 nm).^{12,17,19} The oxidized NPs were examined by STEM (Figures 2d and S12–S16), and the particle diameters were found to be slightly larger than the metallic precursor NPs. The Cu@Str particles increased in diameter from 5 to 6 nm upon oxidation, consistent with the lattice expansion required to form Cu₂O.⁵⁸ However, the ultrasmall Cu@DOPA NPs underwent slightly greater growth, with diameters increasing from 2 to 5 nm after oxidation (Figure 2a,d), presumably because very small NPs have a generally larger driving force for ripening (see Figure 7). After 8 weeks aging under air, the diameters and size distributions of a sample of Cu₂O@DOPA NP were broadly similar to those obtained directly after oxidation, showing only minor ripening of the smaller particles (Figure S17). It appears that the oxidation process can result in bimodal size distributions of the Cu₂O NP products (Figures S13 and S17); this is perhaps due to some coalescence of smaller particles.⁵⁹ The barrier to coalescence may be lowered on oxidation either due to weaker

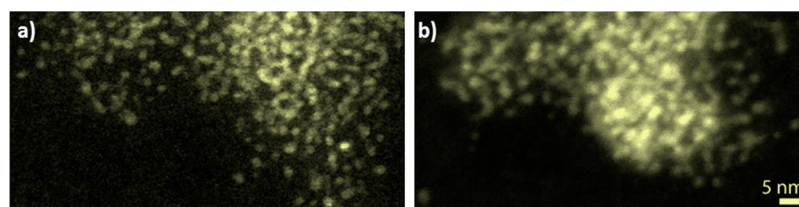


Figure 4. ADF-STEM images of $\text{Cu}_2\text{O}@L$ derived from the direct oxidation of CuMes + ligand ($L-H$), (a) $L = [\text{Str}]^-$, (b) $L = [\text{DOPA}]^-$. Both images shown at the same scale.

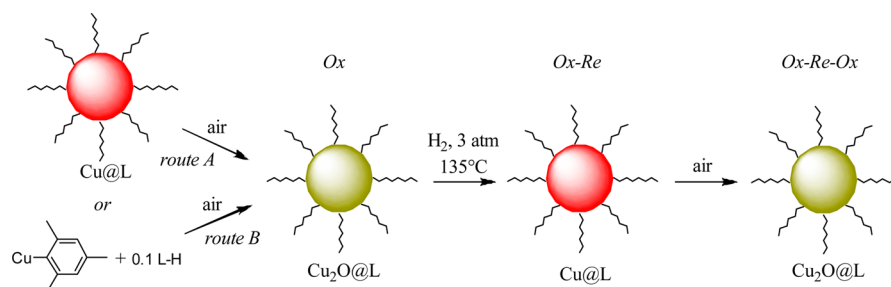


Figure 5. General scheme showing sequential oxidation, reduction, and oxidation steps, where $L = \text{stearate}$ or $\text{di(octyl)phosphinate}$.

ligand binding or the particle expansion, which is likely to reduce ligand coverage of the surface (see [Supporting Note 2](#)).

XPS measurements using $\text{Cu}_2\text{O}@L$ NPs indicated that both Cu(I) and Cu(II) species were present ([Figures 3](#) and [S11](#)). A clear contribution from Cu(II) to the $\text{Cu } 2p$ core level was observed, and a shoulder on the higher BE side of the main core line (Cu(0) or Cu(I)) was visible at a BE of 934.1 eV; both findings agree well with values reported in the literature.⁵⁶ In addition, characteristic shakeup satellites of Cu(II) were found at approximately 7 eV above the main core line, which originate from $\text{O } 2p \rightarrow \text{Cu } 3d$ charge transfer.^{60,61} The $\text{Cu } L_{3M_{4,5}M_{4,5}}$ Auger line was shifted by 1.6 eV to higher BE, compared to the metallic Cu@Str sample, now coinciding with the most intense feature of the Auger line for Cu_2O .^{60,62} In other XPS studies of Cu_2O NPs, similar trends were attributed to an amorphous monolayer of CuO (~ 0.5 nm) over a Cu_2O core.^{24,37,63} While such a thin layer might not be detected by XRD or STEM, an alternative explanation in the current experiments is the presence of ligated Cu(II) surface species. Since the structure of Cu_2O contains only two-coordinate Cu centers,²⁵ those on the surface may be poorly stabilized and easily oxidized. These surface Cu(II) sites may be coordinated either to ligand or adventitious hydroxide; the steric bulk of the ligands is expected to leave plenty of surface copper atoms available for bonding to smaller hydroxide groups.

The IR spectrum of the $\text{Cu}_2\text{O}@L$ NPs revealed two signals for the carboxylate ligands at 1547 and 1410 cm^{-1} , which are assigned to the ligands coordinating in a chelating and delocalized binding mode to the NP surface ([Figure S18](#)). The ligands were also identified by broad signals in the NMR spectra ([Figures S21](#) and [S22](#)).^{5,64,65} There were also broad IR signals at ~ 3270 cm^{-1} which were attributed to surface hydroxide bonds since the signal is not diminished after 24 h under vacuum.

Cu_2O NPs Synthesized Directly from CuMes . As small, well-defined colloids of Cu_2O NPs are themselves an interesting target, their direct formation from the organo-metallic precursor was also investigated ([Figures 1](#) and [5](#)). Exposure of a mesitylene solution of CuMes ($[\text{CuMes}] = 0.036$ M) to air, in the presence of 0.1 molar equiv of ligand, resulted

in the gradual formation of a dark yellow solution of $\text{Cu}_2\text{O}@L$ NPs. On following the reaction with NMR spectroscopy, the CuMes signals⁶⁶ slowly disappeared and the formation of some mesitylene and minor quantities of other organic compounds were observed ([Figures S23–S25](#)).⁶⁷ When using $[\text{DOPA}]^-$, ^{31}P NMR spectroscopy showed the intermediate formation of “ Cu–DOPA ” complexes, as sharp signals, which were lost after several days; only very broadened signals remained, consistent with $\text{Cu}_2\text{O}@L$ ([Figure S25](#)).

The $\text{Cu}_2\text{O}@L$ NPs were isolated by centrifugation of the reaction mixture, and elemental analysis results were consistent with expected values. STEM analysis showed ultrasmall NPs with diameters from 1 to 3 nm ([Figures 4](#) and [S26–S28](#), [Supporting Notes 3](#) and [4](#)). Such exceptionally small particles are likely to be coordinated by a less than complete ligand monolayer (expected particle diameters with a monolayer coverage are 4.5–6 nm; see [Supporting Note 2](#)), which is relevant for many applications of Cu_2O NPs. Powder XRD analysis of $\text{Cu}_2\text{O}@L$ NPs showed only a single very broad peak indexed against the (111) signal for Cu_2O with an implied crystallite size of ~ 1 nm ([Figure S29](#)).³⁷ The FTIR spectra of the NPs were similar to those obtained for the NPs synthesized by oxidation of the Cu@L NPs, confirming ligand and hydroxide surface coordination ([Figures S19](#) and [S20](#)). It is quite surprising, and potentially very useful, that the straightforward synthetic procedure of exposing CuMes and low loadings of ligands to air results in formation of ultrasmall Cu_2O NPs directly.

Reduction of Cu_2O NPs To Form Metallic Cu NPs. The $\text{Cu}_2\text{O}@L$ NPs, both those prepared indirectly by oxidation of Cu NPs (route A, [Figure 5](#)) or formed directly from CuMes (route B, [Figure 5](#)), were successfully reduced to Cu@L NPs by reaction with ~ 3 bar H_2 at 135 °C (lower temperatures, e.g., 110 °C, proved ineffective) ([Figure 5](#)). The resulting red solutions showed typical SPR signals for metallic copper (SPR max = 565–571 nm) in the visible spectra. It is interesting that the water which must be produced upon reduction of Cu_2O does not appear to affect the reaction or products. In fact, addition of degassed water to a solution of (independently synthesized) Cu@Str NPs did not change the UV–vis

spectrum; the lack of sensitivity to the water byproduct is an important result for successful repeated redox cycling.⁶⁸ A sample of Cu@DOPA, produced by reduction of Cu₂O NPs (prepared by route B, Figure 5) was analyzed by air-sensitive TEM techniques (Figure S30). The NPs showed larger diameters (~3–5 nm) compared to those of the ultrasmall Cu₂O precursor NPs (1–3 nm), indicating that the reduction reaction may also trigger some ripening in these very small NPs.

Redox Switching Using Cu/Cu₂O NPs. As both oxidation of Cu NPs and reduction of Cu₂O NPs can be easily achieved, repeated redox cycling was explored. Starting *via* route A (Figure 5), samples were investigated by STEM and visible spectroscopy at each stage of redox cycling (Figures 6 and

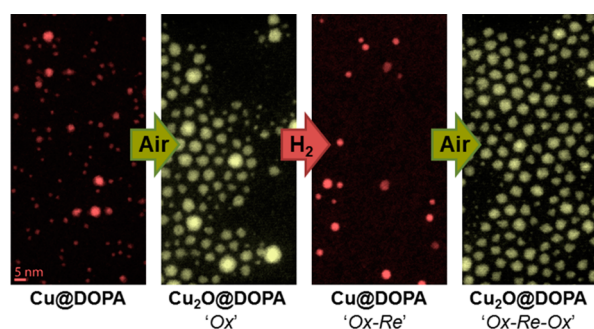


Figure 6. STEM images of Cu@DOPA NPs and the products of oxidizing the sample (to Cu₂O@DOPA), further reduction, and oxidation. All images to the same scale.

S31); solubilized NPs were retained throughout. The initially very small Cu@DOPA particles grew upon the first oxidation (from 2 to 5 nm), but subsequent changes in size were consistent with the oxidative contraction/expansion expected upon changing between Cu₂O and Cu particles (Figures 6 and 7e). The Cu@Str NPs were initially found to be larger (5 nm), and the changes in size upon redox cycling were dominated by the phase change expansion/contraction, although a gradual

underlying trend toward larger particles was also identified (Figure 7b).

To understand the ligand loading effects, a variety of redox sequences were compared using 0.1 and 0.2 equiv of ligand *versus* metal (molar equiv of precursor compounds) and studied by STEM techniques (Figures 7 and S32–S37). The Cu@L NPs prepared using 0.2 equiv of ligand showed very weak SPR signals, consistent with a majority of ultrasmall particles (<2 nm) which are not expected to exhibit a SPR (Figure S9).⁶⁹ The oxidized samples with 0.2 equiv of ligand showed very small (1–3 nm) Cu₂O NPs by STEM analysis, in line with the greater proportion of available ligand (Figures S13, S15, S28, S34, and S35). All NPs ligated by [Str][−] were slightly bigger than their analogues with phosphinate, likely due to the smaller expected surface profile of [Str][−] compared to that of bulkier [DOPA][−] (which has two alkyl chains),⁷⁰ thus requiring a greater number of [Str][−] ligands to cover the same particle surface area (also see Supporting Note 5).

Small Cu NPs, showing average diameters <4 nm, oxidized directly to Cu₂O NPs (Figure 8c), accompanied by a color change from red to pale yellow and the immediate loss of the SPR signal in the visible spectrum (Figure 8a). However, for larger Cu NPs (average diameters >4 nm), the visible spectra suggest the formation of core–shell Cu@Cu₂O NP intermediates during oxidation (Figure 8b).^{12,13,17–22} In samples containing some larger particles (>6 nm), the SPR resonance initially increased in intensity upon oxidation (with a slight red shift), attributed to the formation of a passivating layer of Cu₂O on the Cu NP which removes surface–solvent interactions that initially dampen the SPR.^{15,17,18} The presence of core–shell particles was confirmed by high-resolution TEM, identifying the phases *via* their characteristic lattice spacings (Figure 8d). It was also observed that the color of the initially oxidized solution served as a reasonable indicator of both size and composition of the NPs: yellow solutions comprised mostly NPs <3 nm; green solutions comprised NPs with 3–6 nm particles, whereas turquoise solutions contained some 6–9 nm particles. Furthermore, the oxidation rate and SPR profile, recorded by visible spectroscopy, were good indications of the

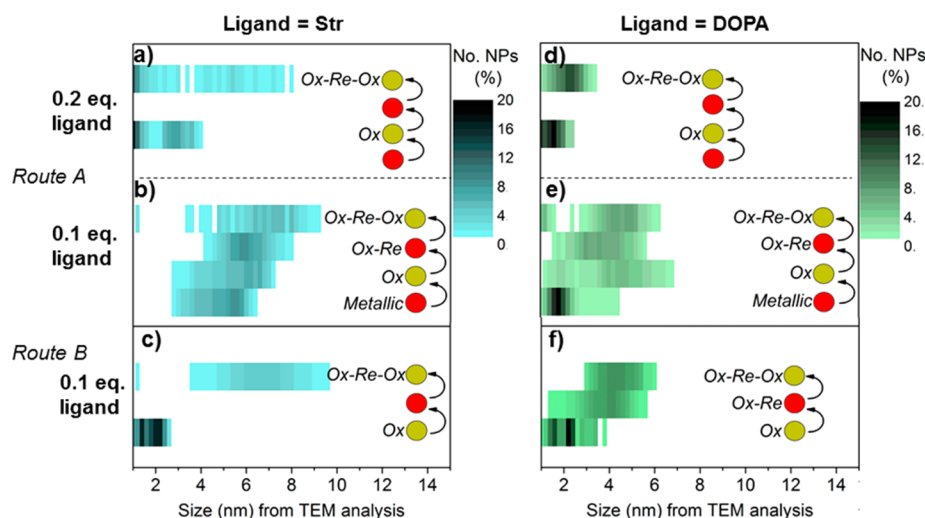


Figure 7. Contour plots showing the size distributions of Cu/Cu₂O NPs (a, 0.2 equiv [Str][−], route A; b, 0.1 equiv [Str][−], route A; c, 0.1 equiv [Str][−], route B; d, 0.2 equiv [DOPA][−], route A; e, 0.1 equiv [DOPA][−], route A; f, 0.1 equiv [DOPA][−], route B) throughout oxidation/reduction cycles. Contours show the percentage of particles that fall within a 0.2 nm diameter size category; N.B. particles smaller than 1 nm were not included in this analysis. Metallic phases analyzed by air-sensitive STEM using vacuum transfer techniques for (b), (e), and (f) only.

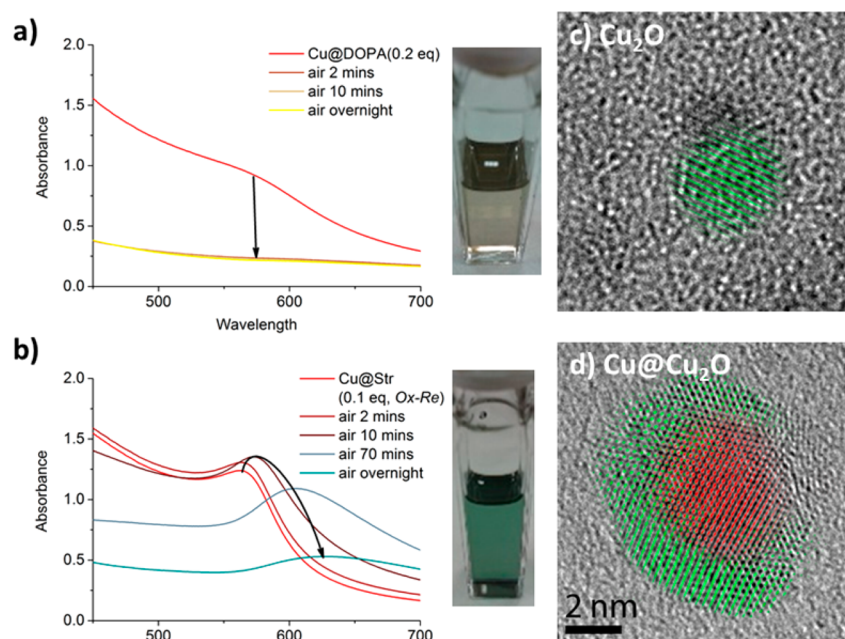


Figure 8. (a,b) Representative visible spectra of Cu NPs before and after exposure to air; (a) shows the rapid oxidation of small Cu@DOPA(0.2 equiv) NPs giving a yellow solution of Cu₂O NPs (~2 nm, Figure S15), and (b) shows the slower oxidation of larger Cu@Str (0.1 equiv, Ox-Re-Ox) NPs to give turquoise Cu@Cu₂O core-shell particles (~8 nm, Figure S32). (c) False color image of a particle from a HRTEM image of a Cu₂O NP (0.2 equiv [DOPA][−], Ox, route A, Figure S15) displaying the Cu₂O (green) 111 lattice spacing. (d) False color image of a particle from HRTEM image of Cu@Cu₂O core-shell particles (0.1 equiv [Str][−], Ox-Re-Ox, route B, Figure S36), displaying the Cu₂O (green) and Cu (red) phases (identified by the lattice spacings).

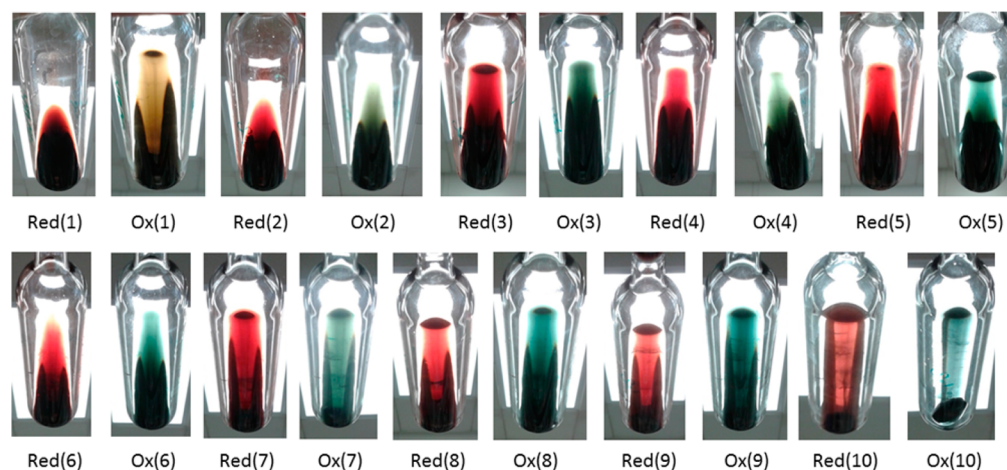


Figure 9. Photographs showing the color of the copper containing colloidal solution throughout 10 reduction and oxidation experiments (red = metallic Cu@DOPA NPs, yellow/green/turquoise = Cu₂O@DOPA NPs or Cu@Cu₂O@DOPA core-shell NPs; 0.2 molar equiv of [DOPA][−] ligand used).

particle size after oxidation, although it should be noted that the larger particles exert a dominating effect on the spectra. After several months under air, the green or turquoise solutions of larger core-shell particles slowly turned to yellow solutions, suggesting that the variation in color arises from the internal metallic Cu core which becomes fully oxidized, leaving only (yellow) Cu₂O, after extended periods (Figure S38).

As the ligand [DOPA][−] was shown to be best for stable size control, a solution of Cu NPs ligated by 0.2 equiv of [DOPA][−] was selected for a multiple redox cycle experiment. The sample was exposed to reduction/oxidation cycles until it had been oxidized a total of 10 times. Remarkably, the solution cycled between red (metallic) and yellow/green/turquoise (oxidized)

reversibly and remained well-dispersed throughout the experiments (Figure 9).

Visible spectroscopy and STEM analysis were recorded after the second, fifth and tenth oxidations (Figure 10). These analyses showed the gradual increase in size of the particles at each stage, but it is striking that the NPs have undergone 19 phase changes in total and have still retained small sizes (<8 nm) and narrow distributions (Figure 10). From the oxidation profiles recorded by visible spectroscopy, the smaller particles converted to a single phase (~3–6 nm Cu₂O NPs) through the first five cycles (although the SPR signal of small <2 nm internal Cu cores may not be resolved by visible spectroscopy) (Figure 10b), but during the 10th oxidation cycle, there was evidence for Cu@Cu₂O core-shell structures (4–8 nm Cu@

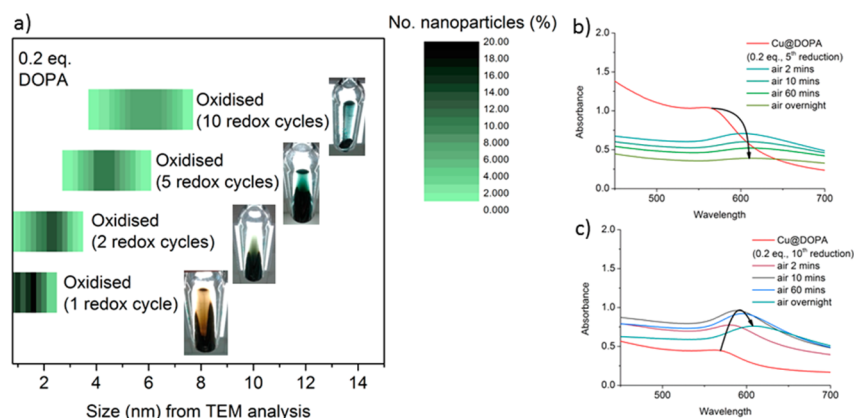


Figure 10. (a) Contour plots showing the size distributions of $\text{Cu}_2\text{O}@DOPA$ (0.2 equiv) NPs throughout 10 reduction/oxidation cycles, with corresponding photographs of the solution at each stage. Contours show the percentage of particles that fall within a 0.2 nm diameter size category; N.B. particles smaller than 1 nm were not included in this analysis. (b,c) Visible spectra of Cu NPs before and after exposure to air, after 5 and 10 cycles.

Cu_2O NPs) (Figure 10c). The findings are consistent with the introduction of the SPR enlargement effect, arising from long-lived core-shell $\text{Cu}@Cu_2\text{O}$ NPs, once some of the particles are sufficiently large (>6 nm). The collected results are consistent with other reports that, upon oxidation, small Cu NPs (<5 nm in size) rapidly lose SPR signal on oxidation,^{12,17,19} while larger (>7 nm) particles initially show an increased SPR signal, indicative of a core-shell arrangement.^{13,17–22}

CONCLUSIONS

Ultrasmall metallic Cu and Cu_2O NPs were prepared as stable colloidal solutions, by reaction of an organo-copper precursor with substoichiometric quantities of monoanionic ligands and subsequent exposure to low pressures of hydrogen gas or to air, respectively. The use of substoichiometric quantities of ligand offers a distinct advantage for processes and applications reliant on surface activity, such as photochemistry, catalysis, or sensing. The absence of excess free ligand also minimizes the presence of an unwanted insulating component for applications in electronics or charge transport, simplifies purification, and is an important step toward allowing nanoparticle formation, *in situ*, within an active device or matrix.⁶⁴ This very straightforward production of exceptionally small Cu_2O NPs may enable a range of applications where high surface area is important. It is also feasible to cycle reversibly between Cu(0) and Cu(I) redox states, by exposure of the NPs to oxidizing (air) or reducing (3 bar H_2) conditions. Thus, NPs can be readily stored and handled in air and reduced under a relatively low pressure of H_2 at the point of use. The ability of a system to rapidly switch between redox states should also prove useful within (photo)-catalytic cycles or for fundamental studies, while understanding of the solution ripening processes involved upon phase change may be applicable to other phase switching nanoparticle systems.⁷¹ Visible spectroscopy and STEM techniques were used to monitor the particles during the redox transitions. By optimizing ligand loading, it was feasible to maintain very small sizes during these redox transitions and to limit any increases in size over the course of at least 19 redox reactions; longer cycling experiments could be pursued in the future. The simple preparation and tailoring of nanoparticle size, redox state, and surface ligand offers a platform of materials for a range of applications in which ultrasmall, narrow size dispersity and soluble NPs are useful. Further exploration of the NPs in fields

spanning catalysis, sensing, optoelectronics, and photonics is recommended.

EXPERIMENTAL METHODS

All manipulations were undertaken using a nitrogen-filled glovebox or using a Schlenk line, unless otherwise stated. Stearic acid was used directly from the supplier; dioctylphosphinic acid⁷² and CuMes⁷⁰ were prepared using established literature routes (N.B. it was essential to filter and recrystallize the CuMes from toluene twice to isolate a very pale yellow powder without any impurities), and CuMes was stored in a glovebox at -20 °C. Mesitylene was degassed by three freeze-pump-thaw cycles and stored under nitrogen over molecular sieves.

NMR spectra were recorded on Bruker AV-400 instruments, and all chemical shifts are reported in parts per million. Solid-state FTIR spectra under air were recorded using a PerkinElmer Spectrum 100 FTIR spectrometer with a Universal ATR sampling accessory. For air-sensitive IR experiments, a Mettler-Toledo ReactIR iC10 probe was immersed in a powdered solid sample under a flow of N_2 . UV/visible spectra of mesitylene solutions diluted with toluene (to $[\text{Cu}] = 1.2$ mM) were collected using PerkinElmer Lambda 950 spectrophotometer. X-ray diffraction was performed using an X'Pert Pro diffractometer (PANalytical B.V., The Netherlands) and X'Pert Data Collector software, version 2.2b. The instrument was used in the θ/θ reflection mode, fitted with a nickel filter, 0.04 rad Soller slit, 10 mm mask, $1/4^\circ$ fixed divergence slit, and $1/2^\circ$ fixed antiscatter slit. Air-sensitive samples were prepared in a glovebox and sealed with adhesive polyimide tape. The diffraction patterns were analyzed using Fitky (version 0.9.0; Marcin Wojdyr, 2010); the peaks were fitted to a SplitPearson7 function, and the crystallite size was calculated using the fitted full width at half-maximum using the Scherrer equation. Scanning TEM images, conventional TEM images, and electron diffraction patterns were acquired on an FEI Titan 80-300 microscope operated at 300 kV or a JEOL 2100-F microscope operated at 200 kV. For air-sensitive samples, the sample solution was deposited on a 400 mesh copper holey carbon grid with an ultrathin 3 nm thick carbon support (Agar Scientific AGS187-4) while in a glovebox. The grid was then loaded into a Gatan vacuum transfer holder to prevent any exposure to air prior to TEM imaging. The same grid was used for non-air-sensitive samples. X-ray photoelectron spectroscopy was recorded on a Thermo Scientific K-Alpha⁺ X-ray photoelectron spectrometer system operating at 2×10^{-9} mbar base pressure. This system incorporates a monochromated, microfocused Al $K\alpha$ X-ray source ($h\nu = 1486.6$ eV) and a 180° double focusing hemispherical analyzer with a 2D detector. The X-ray source was operated with a 6 mA emission current and 12 kV anode bias. Data were collected at 20 eV pass energy using an X-ray spot size of $400 \mu\text{m}^2$. A flood gun was used to minimize sample charging. Samples were mounted using conductive carbon tape, and air-sensitive samples were transferred to

the spectrometer using a special glovebox module which ensured that they were never exposed to air. All XPS data were analyzed using the Advantage software package.

Synthesis of Cu@L NPs. The dry ligand (stearic acid or dioctylphosphinic acid) and CuMes were added to a Young's tap flask in a glovebox, and mesitylene was added to make up the concentration to $[\text{CuMes}] = 0.036 \text{ M}$. The solution was stirred for 10 min and was almost colorless. The solution was degassed, by freeze–pump–thaw methods, to remove the N_2 atmosphere and the solution refrozen and evacuated before addition of H_2 gas at 1 bar for 30 s (open to bubbler). By submerging 2/3 of the flask in liquid N_2 during the addition of H_2 , a pressure of ~ 3 bar can be achieved once the sealed flask is warmed to room temperature. After the flask had warmed to room temperature, it was placed in a prewarmed oil bath at 110°C and stirred for 2.5 h to give a deep red solution (Supporting Note 1). After this period, the flask was left to cool and the H_2 removed by four cycles of short vacuum/ N_2 ; care was taken not to remove solvent during the degassing process. The samples were then stored in vials in a glovebox where they remained red and well-dispersed for several weeks. N.B. Larger volume reactions may require longer reduction times to consume all starting material. N.B. Reduction of CuMes in the absence of ligands is rather slow (and forms a Cu mirror rather than a colloid). Elemental analysis of dried samples (all solvents and volatiles removed): Cu@DOPA(0.1 equiv) calcd (%) C, 20.79; H, 3.71; found (%) C, 20.79; H, 3.91; Cu@Str (0.1 equiv) calcd (%) C, 23.54; H, 3.84; found (%) C, 25.95; H, 4.49%.

Oxidation of Cu@NPs. Cu@L NPs oxidize upon exposure to air; representative color photos displayed with visible spectra were recorded after 24 h under air. UV/vis spectra were recorded by collecting 100 μL of the original Cu@L NP solution and adding 2.9 mL of toluene to give a solution with $[\text{Cu}] = 1.2 \text{ mM}$ in a quartz cuvette ($\sim 0.1 \text{ mL}$ of air required for stoichiometric oxidation); this was tightly sealed by applying Teflon tape to the screw seal to ensure an air-free environment. After initial analysis of the Cu NPs, the lid was removed and the solution exposed to air for 30 s, resealed, and shaken vigorously for 30 s (then the process was repeated once more). The exposed solution was then monitored by visible spectroscopy (2 min air) and again periodically (10 min, 60 min, and after 24 h).

Direct Synthesis of Cu_2O @L NPs. The dry ligand (stearic acid or dioctylphosphinic acid) and CuMes were added to a Young's tap flask in a glovebox, and then mesitylene was added to make up the concentration to $[\text{CuMes}] = 0.036 \text{ M}$. The flask was then exposed to air while stirring and left unsealed for 3 days. The resulting yellow/brown colloidal solution remained dispersed while being stirred but partially precipitated at this concentration if left static; if diluted, the solution is well-dispersed. Elemental analysis of dried samples (after centrifugation): Cu_2O @DOPA(0.1 equiv) calcd (%) C, 19.13; H, 3.41; found (%) C, 24.23; H, 4.78; Cu_2O @Str (0.1 equiv) calcd (%) C, 21.65; H, 3.53; found (%) C, 23.08; H, 4.69. The larger than expected hydrogen content may be explained by surface hydroxide/adsorbed water.

Reduction of Cu_2O @L NPs. Solutions of Cu_2O NPs ($[\text{Cu}] = 0.036 \text{ M}$) were freeze/thaw degassed twice to remove any air, and the solution was refrozen and evacuated before addition of H_2 gas at 1 bar for 30 s (open to bubbler). By submerging 2/3 of the flask in liquid N_2 during the addition of H_2 , a pressure of ~ 3 bar can be achieved once the sealed flask is warmed to room temperature. After the flask had warmed to room temperature, it was placed in a prewarmed oil bath at 135°C and stirred for 50 min to give a deep red solution. After this period, the flask was left to cool and the H_2 removed by four cycles of short vacuum/ N_2 .

TEM Sizing Procedure. Cu and Cu_2O NP sizes were measured by analyzing ADF-STEM images, which had a NP signal-to-background ratio higher than that with conventional TEM images [especially for small ($<3 \text{ nm}$) NPs]. The total dose per NP was also much lower with ADF-STEM, which minimized any NP size change resulting from reduction under the electron beam (see Supporting Note 4). An intensity threshold for each ADF-STEM image was chosen using the ImageJ software to isolate pixels containing signal from NPs from the

carbon substrate background. After applying the threshold, we used the “Despeckle” operation to reduce noise, and the area of each NP was then measured using the “Analyze Particles” function with a circularity condition between 0.5 and 0.7, depending on the sample. The NPs were assumed to be spherical, and their diameters were calculated from the measured area. For most samples, at least several hundred (up to 20 000) NPs were measured; the exceptionally small Cu_2O NPs ($<3 \text{ nm}$) were difficult to measure, and a lower sample number was analyzed in these cases. To ensure a threshold choice that accurately selected pixels corresponding to NPs, the resulting processed image was compared with the original ADF-STEM image. After applying each threshold method within ImageJ,⁷³ we chose the appropriate method by comparing each result with line profiles drawn across several NPs of representative sizes on the original image. The choice of method changed depending on the number density of NPs in the image, the size distribution, and signal-to-noise. In images with either bimodal distributions or a wide range of NP sizes, a single threshold could be inappropriate: a substantial number of NPs were either not recognized or inaccurately measured. In these cases, two thresholds were used with a size cutoff (*i.e.*, one threshold for small NPs, another choice for large). Comparing measurements using different method choices on several images with different size distributions, we estimate systematic errors introduced using this automated analysis routine are less than 5%.

ASSOCIATED CONTENT

Supporting Information

The Supporting Information is available free of charge on the ACS Publications website at DOI: 10.1021/acsnano.6b07694.

NMR, FTIR, X-ray photoelectron and visible spectra, XRD patterns, TEM images, and full particle size analysis (PDF)

AUTHOR INFORMATION

Corresponding Authors

*E-mail: charlotte.williams@chem.ox.ac.uk.

*E-mail: m.shaffer@imperial.ac.uk.

ORCID

Sebastian D. Pike: 0000-0002-9791-5244

Anna Regoutz: 0000-0002-3747-3763

Charlotte K. Williams: 0000-0002-0734-1575

Notes

The authors declare no competing financial interest.

ACKNOWLEDGMENTS

The EPSRC are acknowledged for funding (EP/K035274/1, EP/M013839/1, EP/H046380/1).

REFERENCES

- (1) Franco, D. F.; Sant'Ana, A. C.; De Oliveira, L. F. C.; Silva, M. A. P. The Sb_2O_3 Redox Route to Obtain Copper Nanoparticles in Glasses with Plasmonic Properties. *J. Mater. Chem. C* **2015**, *3*, 3803–3808.
- (2) Magdassi, S.; Grouchko, M.; Kamyshny, A. Copper Nanoparticles for Printed Electronics: Routes Towards Achieving Oxidation Stability. *Materials* **2010**, *3*, 4626.
- (3) Jeong, S.; Woo, K.; Kim, D.; Lim, S.; Kim, J. S.; Shin, H.; Xia, Y.; Moon, J. Controlling the Thickness of the Surface Oxide Layer on Cu Nanoparticles for the Fabrication of Conductive Structures by Ink-Jet Printing. *Adv. Funct. Mater.* **2008**, *18*, 679–686.
- (4) Li, W.; Chen, M. Synthesis of Stable Ultra-Small Cu Nanoparticles for Direct Writing Flexible Electronics. *Appl. Surf. Sci.* **2014**, *290*, 240–245.
- (5) Brown, N. J.; Weiner, J.; Hellgardt, K.; Shaffer, M. S. P.; Williams, C. K. Phosphinate Stabilised ZnO and Cu Colloidal Nanocatalysts for

- CO₂ Hydrogenation to Methanol. *Chem. Commun.* **2013**, 49, 11074–11076.
- (6) Schimpf, S.; Rittermeier, A.; Zhang, X.; Li, Z.-A.; Spasova, M.; van den Berg, M. W. E.; Farle, M.; Wang, Y.; Fischer, R. A.; Muhler, M. Stearate-Based Cu Colloids in Methanol Synthesis: Structural Changes Driven by Strong Metal–Support Interactions. *ChemCatChem* **2010**, 2, 214–222.
- (7) d'Halluin, M.; Mabit, T.; Fairley, N.; Fernandez, V.; Gawande, M. B.; Le Grogne, E.; Felpin, F.-X. Graphite-Supported Ultra-Small Copper Nanoparticles – Preparation, Characterization and Catalysis Applications. *Carbon* **2015**, 93, 974–983.
- (8) Park, J. B.; Graciani, J.; Evans, J.; Stacchiola, D.; Senanayake, S. D.; Barrio, L.; Liu, P.; Sanz, J. F.; Hrbek, J.; Rodriguez, J. A. Gold, Copper, and Platinum Nanoparticles Dispersed on CeO_x/TiO₂(110) Surfaces: High Water-Gas Shift Activity and the Nature of the Mixed-Metal Oxide at the Nanometer Level. *J. Am. Chem. Soc.* **2010**, 132, 356–363.
- (9) Jin, T.; Yan, M.; Yamamoto, Y. Click Chemistry of Alkyne–Azide Cycloaddition using Nanostructured Copper Catalysts. *ChemCatChem* **2012**, 4, 1217–1229.
- (10) Gonzalez-Arellano, C.; Luque, R.; Macquarrie, D. J. Microwave Efficient S-Arylation of Thiols with Aryl Iodides Using Supported Metal Nanoparticles. *Chem. Commun.* **2009**, 1410–1412.
- (11) Kim, B. H.; Hackett, M. J.; Park, J.; Hyeon, T. Synthesis, Characterization, and Application of Ultrasmall Nanoparticles. *Chem. Mater.* **2014**, 26, 59–71.
- (12) Kanninen, P.; Johans, C.; Merta, J.; Kontturi, K. Influence of Ligand Structure on the Stability and Oxidation of Copper Nanoparticles. *J. Colloid Interface Sci.* **2008**, 318, 88–95.
- (13) Glaria, A.; Cure, J.; Piettre, K.; Coppel, Y.; Turrin, C.-O.; Chaudret, B.; Fau, P. Deciphering Ligands' Interaction with Cu and Cu₂O Nanocrystal Surfaces by NMR Solution Tools. *Chem. - Eur. J.* **2015**, 21, 1169–1178.
- (14) Sun, Q.-C.; Ding, Y.; Goodman, S. M.; Funke, H. H.; Nagpal, P. Copper Plasmonics and Catalysis: Role of Electron-Phonon Interactions in Dephasing Localized Surface Plasmons. *Nanoscale* **2014**, 6, 12450–12457.
- (15) Peña-Rodríguez, O.; Pal, U. Effects of Surface Oxidation on the Linear Optical Properties of Cu Nanoparticles. *J. Opt. Soc. Am. B* **2011**, 28, 2735–2739.
- (16) Rice, K. P.; Paterson, A. S.; Stoykovich, M. P. Nanoscale Kirkendall Effect and Oxidation Kinetics in Copper Nanocrystals Characterized by Real-Time, In Situ Optical Spectroscopy. *Part. Part. Syst. Char.* **2015**, 32, 373–380.
- (17) Barriere, C.; Piettre, K.; Latour, V.; Margeat, O.; Turrin, C.-O.; Chaudret, B.; Fau, P. Ligand Effects on the Air Stability of Copper Nanoparticles Obtained from Organometallic Synthesis. *J. Mater. Chem.* **2012**, 22, 2279–2285.
- (18) Rice, K. P.; Walker, E. J.; Stoykovich, M. P.; Saunders, A. E. Solvent-Dependent Surface Plasmon Response and Oxidation of Copper Nanocrystals. *J. Phys. Chem. C* **2011**, 115, 1793–1799.
- (19) Cheng, G.; Hight Walker, A. R. Transmission Electron Microscopy Characterization of Colloidal Copper Nanoparticles and their Chemical Reactivity. *Anal. Bioanal. Chem.* **2010**, 396, 1057–1069.
- (20) Uk Son, S.; Kyu Park, I.; Park, J.; Hyeon, T. Synthesis of Cu₂O Coated Cu Nanoparticles and their Successful Applications to Ullmann-Type Amination Coupling Reactions of Aryl Chlorides. *Chem. Commun.* **2004**, 778–779.
- (21) Schröter, M. K.; Khodeir, L.; Hambrock, J.; Löffler, E.; Muhler, M.; Fischer, R. A. Redox Chemistry of Cu Colloids Probed by Adsorbed CO: An In Situ Attenuated Total Reflection Fourier Transform Infrared Study. *Langmuir* **2004**, 20, 9453–9455.
- (22) Hung, L.-I.; Tsung, C.-K.; Huang, W.; Yang, P. Room-Temperature Formation of Hollow Cu₂O Nanoparticles. *Adv. Mater.* **2010**, 22, 1910–1914.
- (23) Chen, K.; Song, S.; Xue, D. Vapor-Phase Crystallization Route to Oxidized Cu Foils in Air as Anode Materials for Lithium-Ion Batteries. *CrystEngComm* **2013**, 15, 144–151.
- (24) Yin, M.; Wu, C.-K.; Lou, Y.; Burda, C.; Koberstein, J. T.; Zhu, Y.; O'Brien, S. Copper Oxide Nanocrystals. *J. Am. Chem. Soc.* **2005**, 127, 9506–9511.
- (25) Meyer, B. K.; Polity, A.; Reppin, D.; Becker, M.; Hering, P.; Klar, P. J.; Sander, T.; Reindl, C.; Benz, J.; Eickhoff, M.; Heiliger, C.; Heinemann, M.; Blasing, J.; Krost, A.; Shokovets, S.; Müller, C.; Ronning, C. Binary Copper Oxide Semiconductors: From Materials Towards Devices. *Phys. Status Solidi B* **2012**, 249, 1487–1509.
- (26) Xu, L.; Jiang, L.-P.; Zhu, J.-J. Sonochemical Synthesis and Photocatalysis of Porous Cu₂O Nanospheres with Controllable Structures. *Nanotechnology* **2009**, 20, 045605.
- (27) Schreier, M.; Luo, J.; Gao, P.; Moehl, T.; Mayer, M. T.; Grätzel, M. Covalent Immobilization of a Molecular Catalyst on Cu₂O Photocathodes for CO₂ Reduction. *J. Am. Chem. Soc.* **2016**, 138, 1938–1946.
- (28) Paracchino, A.; Laporte, V.; Sivula, K.; Grätzel, M.; Thimsen, E. Highly Active Oxide Photocathode for Photoelectrochemical Water Reduction. *Nat. Mater.* **2011**, 10, 456–461.
- (29) Singhal, A.; Pai, M. R.; Rao, R.; Pillai, K. T.; Lieberwirth, I.; Tyagi, A. K. Copper(I) Oxide Nanocrystals – One Step Synthesis, Characterization, Formation Mechanism, and Photocatalytic Properties. *Eur. J. Inorg. Chem.* **2013**, 2013, 2640–2651.
- (30) Wadia, C.; Alivisatos, A. P.; Kammen, D. M. Materials Availability Expands the Opportunity for Large-Scale Photovoltaics Deployment. *Environ. Sci. Technol.* **2009**, 43, 2072–2077.
- (31) Rai, B. P. Cu₂O Solar Cells: A Review. *Sol. Cells* **1988**, 25, 265–272.
- (32) Li, J.-H.; Tang, B.-X.; Tao, L.-M.; Xie, Y.-X.; Liang, Y.; Zhang, M.-B. Reusable Copper-Catalyzed Cross-Coupling Reactions of Aryl Halides with Organotins in Inexpensive Ionic Liquids. *J. Org. Chem.* **2006**, 71, 7488–7490.
- (33) Kessler, M. T.; Robke, S.; Sahler, S.; Precht, M. H. G. Ligand-Free Copper(I) Oxide Nanoparticle-Catalysed Amination of Aryl Halides in Ionic Liquids. *Catal. Sci. Technol.* **2014**, 4, 102–108.
- (34) Zhang, J.; Liu, J.; Peng, Q.; Wang, X.; Li, Y. Nearly Monodisperse Cu₂O and CuO Nanospheres: Preparation and Applications for Sensitive Gas Sensors. *Chem. Mater.* **2006**, 18, 867–871.
- (35) Michael, J. J.; Iniyan, S. Performance of Copper Oxide/Water Nanofluid in a Flat Plate Solar Water Heater Under Natural and Forced Circulations. *Energy Convers. Manage.* **2015**, 95, 160–169.
- (36) Palkar, V. R.; Ayyub, P.; Chattopadhyay, S.; Multani, M. Size-Induced Structural Transitions in the Cu–O and Ce–O Systems. *Phys. Rev. B: Condens. Matter Mater. Phys.* **1996**, 53, 2167–2170.
- (37) Borgohain, K.; Murase, N.; Mahamuni, S. Synthesis and Properties of Cu₂O Quantum Particles. *J. Appl. Phys.* **2002**, 92, 1292–1297.
- (38) Yanase, A.; Komiyama, H. In Situ Observation of Oxidation and Reduction of Small Supported Copper Particles Using Optical Absorption and X-ray Diffraction. *Surf. Sci.* **1991**, 248, 11–19.
- (39) Yanase, A.; Komiyama, H. Real-Time Optical Observation of Morphological Change of Small Supported Copper Particles During Redox Treatments. *Surf. Sci.* **1991**, 248, 20–26.
- (40) Li, C. W.; Ciston, J.; Kanan, M. W. Electroreduction of Carbon Monoxide to Liquid Fuel on Oxide-Derived Nanocrystalline Copper. *Nature* **2014**, 508, 504–507.
- (41) Holse, C.; Elkjær, C. F.; Nierhoff, A.; Sehested, J.; Chorkendorff, I.; Helveg, S.; Nielsen, J. H. Dynamic Behavior of CuZn Nanoparticles under Oxidizing and Reducing Conditions. *J. Phys. Chem. C* **2015**, 119, 2804–2812.
- (42) Nishida, N.; Miyashita, A.; Hashimoto, N.; Murayama, H.; Tanaka, H. Regenerative Synthesis of Copper Nanoparticles by Photoirradiation. *Eur. Phys. J. D* **2011**, 63, 307.
- (43) Song, J.; Rodenbough, P. P.; Xu, W.; Senanayake, S. D.; Chan, S.-W. Reduction of Nano-Cu₂O: Crystallite Size Dependent and the Effect of Nano-Ceria Support. *J. Phys. Chem. C* **2015**, 119, 17667–17672.
- (44) Behrens, M.; Schlögl, R. How to Prepare a Good Cu/ZnO Catalyst or the Role of Solid State Chemistry for the Synthesis of

Nanostructured Catalysts. *Z. Anorg. Allg. Chem.* **2013**, 639, 2683–2695.

(45) Tarasov, A.; Kühl, S.; Schumann, J.; Behrens, M. Thermokinetic Study of the Reduction Process of a CuO/ZnAl₂O₄ Catalyst. *High Temp. High Press.* **2013**, 42, 377.

(46) Kalakkad, D.; Anderson, S. L.; Logan, A. D.; Pena, J.; Braunschweig, E. J.; Peden, C. H. F.; Datye, A. K. n-Butane Hydrogenolysis as a Probe of Surface Sites in Rhodium Metal Particles: Correlation with Single Crystals. *J. Phys. Chem.* **1993**, 97, 1437–1444.

(47) Datye, A. K.; Bravo, J.; Nelson, T. R.; Atanasova, P.; Lyubovsky, M.; Pfefferle, L. Catalyst Microstructure and Methane Oxidation Reactivity During the Pd \leftrightarrow PdO Transformation on Alumina Supports. *Appl. Catal., A* **2000**, 198, 179–196.

(48) Ono, L. K.; Croy, J. R.; Heinrich, H.; Roldan Cuenya, B. Oxygen Chemisorption, Formation, and Thermal Stability of Pt Oxides on Pt Nanoparticles Supported on SiO₂/Si(001): Size Effects. *J. Phys. Chem. C* **2011**, 115, 16856–16866.

(49) Datye, A. K. Electron Microscopy of Catalysts: Recent Achievements and Future Prospects. *J. Catal.* **2003**, 216, 144–154.

(50) Cabot, A.; Puentes, V. F.; Shevchenko, E.; Yin, Y.; Balcells, L.; Marcus, M. A.; Hughes, S. M.; Alivisatos, A. P. Vacancy Coalescence during Oxidation of Iron Nanoparticles. *J. Am. Chem. Soc.* **2007**, 129, 10358–10360.

(51) Ha, D.-H.; Moreau, L. M.; Honrao, S.; Hennig, R. G.; Robinson, R. D. The Oxidation of Cobalt Nanoparticles into Kirkendall-Hollowed CoO and Co₃O₄: The Diffusion Mechanisms and Atomic Structural Transformations. *J. Phys. Chem. C* **2013**, 117, 14303–14312.

(52) Railsback, J. G.; Johnston-Peck, A. C.; Wang, J.; Tracy, J. B. Size-Dependent Nanoscale Kirkendall Effect During the Oxidation of Nickel Nanoparticles. *ACS Nano* **2010**, 4, 1913–1920.

(53) Bunge, S. D.; Boyle, T. J.; Headley, T. J. Synthesis of Coinage-Metal Nanoparticles from Mesityl Precursors. *Nano Lett.* **2003**, 3, 901–905.

(54) Barriere, C.; Alcaraz, G.; Margeat, O.; Fau, P.; Quoirin, J. B.; Anceau, C.; Chaudret, B. Copper Nanoparticles and Organometallic Chemical Liquid Deposition (OMCLD) for Substrate Metallization. *J. Mater. Chem.* **2008**, 18, 3084–3086.

(55) Brown, N. J.; Garcia-Trencó, A.; Weiner, J.; White, E. R.; Allinson, M.; Chen, Y.; Wells, P. P.; Gibson, E. K.; Hellgardt, K.; Shaffer, M. S. P.; Williams, C. K. From Organometallic Zinc and Copper Complexes to Highly Active Colloidal Catalysts for the Conversion of CO₂ to Methanol. *ACS Catal.* **2015**, 5, 2895–2902.

(56) Tahir, D.; Tougaard, S. Electronic and Optical Properties of Cu, CuO and Cu₂O Studied by Electron Spectroscopy. *J. Phys.: Condens. Matter* **2012**, 24, 175002.

(57) Hu, J. P.; Payne, D. J.; Egde, R. G.; Glans, P. A.; Learmonth, T.; Smith, K. E.; Guo, J.; Harrison, N. M. On-Site Interband Excitations in Resonant Inelastic X-ray Scattering from Cu₂O. *Phys. Rev. B: Condens. Matter Mater. Phys.* **2008**, 77, 155115.

(58) Nakamura, R.; Tokozakura, D.; Nakajima, H.; Lee, J.-G.; Mori, H. Hollow Oxide Formation by Oxidation of Al and Cu Nanoparticles. *J. Appl. Phys.* **2007**, 101, 074303.

(59) Bayram, E.; Lu, J.; Aydin, C.; Browning, N. D.; Özkar, S.; Finney, E.; Gates, B. C.; Finke, R. G. Agglomerative Sintering of an Atomically Dispersed Ir1/Zeolite Y Catalyst: Compelling Evidence Against Ostwald Ripening but for Bimolecular and Autocatalytic Agglomeration Catalyst Sintering Steps. *ACS Catal.* **2015**, 5, 3514–3527.

(60) Panzner, G.; Egert, B.; Schmidt, H. P. The Stability of CuO and Cu₂O Surfaces During Argon Sputtering Studied by XPS and AES. *Surf. Sci.* **1985**, 151, 400–408.

(61) Scrocco, M. Satellite Structure in the X-ray Photoelectron Spectra of CuO Cu₂O. *Chem. Phys. Lett.* **1979**, 63, 52–56.

(62) Larson, P. E. X-ray Induced Photoelectron and Auger Spectra of Cu, CuO, Cu₂O, and Cu₂S Thin Films. *J. Electron Spectrosc. Relat. Phenom.* **1974**, 4, 213–218.

(63) Wu, C.-K.; Yin, M.; O'Brien, S.; Koberstein, J. T. Quantitative Analysis of Copper Oxide Nanoparticle Composition and Structure by

X-ray Photoelectron Spectroscopy. *Chem. Mater.* **2006**, 18, 6054–6058.

(64) Orchard, K. L.; Shaffer, M. S. P.; Williams, C. K. Organometallic Route to Surface-Modified ZnO Nanoparticles Suitable for In Situ Nanocomposite Synthesis: Bound Carboxylate Stoichiometry Controls Particle Size or Surface Coverage. *Chem. Mater.* **2012**, 24, 2443–2448.

(65) Nakamoto, K. *Infrared and Raman Spectroscopy of Inorganic and Coordination Compounds Part B: Applications on Coordination, Organometallic, and Bioinorganic Chemistry*, 5th ed.; John Wiley & Sons: New York, 1997.

(66) Stollenz, M.; Meyer, F. Mesitylcopper – A Powerful Tool in Synthetic Chemistry. *Organometallics* **2012**, 31, 7708–7727.

(67) Reaction of CuMes with moisture releases mesitylene, whereas reaction with O₂ may result in different organic byproducts; for example, the partial oxygenation of CuMes generates bimesityl. See: Haakansson, M.; Oertendahl, M.; Jagner, S.; Sigalas, M. P.; Eisenstein, O. Splitting Dioxygen with Mesitylcopper(I). An Arylcopper(I) Intermediate, Formed in a Coupling Reaction, Containing Two Trapped Trigonal Pyramidal Coordinated Oxides. *Inorg. Chem.* **1993**, 32 (10), 2018–2024.

(68) Yagi, S. Potential-pH Diagrams for Oxidation-State Control of Nanoparticles Synthesized via Chemical Reduction. In *Thermodynamics - Physical Chemistry of Aqueous Systems*; Moreno-Pirajan, J. C., Ed.; InTech, 2011.

(69) Ghodselahi, T.; Vesaghi, M. A.; Shafiekhani, A. Study of Surface Plasmon Resonance of Cu@Cu₂O Core–Shell Nanoparticles by Mie Theory. *J. Phys. D: Appl. Phys.* **2009**, 42, 015308.

(70) Meyer, E. M.; Gambarotta, S.; Floriani, C.; Chiesi-Villa, A.; Guastini, C. Polynuclear Aryl Derivatives of Group 11 Metals. Synthesis, Solid State-Solution Structural Relationship, and Reactivity with Phosphines. *Organometallics* **1989**, 8, 1067–1079.

(71) Bordet, A.; Lacroix, L.-M.; Soulantica, K.; Chaudret, B. A New Approach to the Mechanism of Fischer–Tropsch Syntheses Arising from Gas Phase NMR and Mass Spectrometry. *ChemCatChem* **2016**, 8, 1727–1731.

(72) Wang, F.; Tang, R.; Buhro, W. E. The Trouble with TOPO; Identification of Adventitious Impurities Beneficial to the Growth of Cadmium Selenide Quantum Dots, Rods, and Wires. *Nano Lett.* **2008**, 8, 3521–3524.

(73) Woehrle, G. H.; Hutchinson, J. E.; Ozkar, S.; Finke, R. G. Analysis of Nanoparticle Transmission Electron Microscopy Data Using a Public-Domain Image-Processing Program, Image. *Turk. J. Chem.* **2006**, 30, 1–13.